# Verification of gyrokinetic particle simulation of current-driven instability in fusion plasmas. IV. Drift-tearing mode

Hao Shi,[1,2,3] Wenlu Zhang,[1,2,3,4,a)] (iD) Hongying Feng,[1,2,3,5] Zhihong Lin,[6] (iD) Chao Dong,[2,3] Jian Bao,[2,3] and Ding Li[1,2,3]

## AFFILIATIONS

[1]Department of Engineering and Applied Physics, University of Science and Technology of China, Hefei, Anhui 230026, China
[2]Beijing National Laboratory for Condensed Matter Physics and CAS Key Laboratory of Soft Matter Physics, Institute of Physics, Chinese Academy of Sciences, Beijing 100190, China
[3]University of Chinese Academy of Sciences, Beijing 100049, China
[4]Songshan Lake Materials Laboratory, Dongguan, Guangdong 523808, China
[5]College of Mechanical and Power Engineering, China Three Gorges University, Yichang, Hubei 443002, China
[6]Department of Physics and Astronomy, University of California, Irvine, California 92697, USA

[a)]Electronic mail: wzhang@iphy.ac.cn. URL: https://www.indac.info.

## ABSTRACT

The drift-tearing instability due to diamagnetic drift effects is verified using the Gyrokinetic Toroidal Code (GTC). First, the classical (2,1) resistive tearing mode is verified in a cylindrical geometry with a fluid model. The dependence of the growth rate of the resistive tearing mode on the beta value of the plasma is obtained and is found to qualitatively agree with the theoretical prediction. A drift-tearing mode is subsequently generated when the equilibrium pressure gradient is significant. In this mode, diamagnetic drift effects result in a reduced growth rate and a real frequency equal to the electron diamagnetic frequency. The scaling relation between the diamagnetic frequency and the growth rate of the drift-tearing mode has been calculated. This relation shows good agreement with the theoretical prediction for a relatively small resistivity; however, an obvious deviation arises when the resistivity is large.

Published under license by AIP Publishing. https://doi.org/10.1063/1.5116332

## I. INTRODUCTION

Tearing modes[1–3] are among the most dangerous instabilities related to magnetohydrodynamics (MHD) in tokamak discharges. They are driven by the magnetic free energy, which is determined by the form of the current profile.[4] They can change the topology of the magnetic field via magnetic reconnection and lead to the formation of magnetic islands, thus enhancing cross field transport and degrading the particle and energy confinement. The disruption triggered by a tearing mode would be catastrophic in a long-pulse fusion plasma device such as the International Thermonuclear Experimental Reactor (ITER).[5,6]

The magnetic reconnection caused by a tearing mode is driven by the magnetic energy difference between the initial and final states. The time scale for mode growth is determined by a combination of the resistive diffusion time $\tau_R$, which is related to the diffusion of magnetic field lines through the plasma, and the Alfvén time $\tau_A$, which is related

to the ideal plasma response.[4] The reconnection time is given by $\tau = S^p \tau_A$, where $S = \tau_R/\tau_A$ is the Lundquist number and the power $p$ varies from zero to one depending on the self-consistent geometry and the driving force. For the $m = 2$, $n = 1$ resistive tearing mode, the driving forces lead to reconnection with $p = 3/5$ in the linear phase when the island width is narrower than the resistive layer thickness.

Much effort has been directed toward studying tearing modes in fusion plasmas over the past few decades, using both MHD[1,3,7,8] and kinetic[9–11] theoretical frameworks for the linear and nonlinear phases. To solve a singular perturbation problem near a rational surface, the boundary layer method is usually applied to separate the problem into two regions: an ideal MHD outer region and an inner region around the rational surface, where the effects of plasma resistivity are significant. The dispersion relation of the tearing mode is derived by matching two solutions for the inner and outer regions. Hazeltine *et al.*[9] developed the kinetic theory for studying the classical tearing mode

using the guiding-center kinetic equation with a Fokker-Planck collision term in a cylindrical geometry. Later, Drake and Lee[10] kinetically investigated the transition of the tearing instability from the collisional to the collisionless regime. Depending on the collisionality of the plasma, the tearing instability can be divided into three regimes: collisionless, semicollisional, and collisional.

It has been shown that in a hot magnetically confined plasma, the diamagnetic drift effects on tearing modes are significant. A cross field pressure gradient can also serve as an energy source driving tearing instabilities when the diamagnetic frequency is higher than the growth rate of the resistive tearing mode. The coupling of drift modes to tearing modes leads to a substantial reduction in the growth rate and the production of a real frequency; for convenience, the resulting modes are called drift-tearing modes. These diamagnetic effects were first investigated kinetically,[9,10] leading to the discovery that the growth rate is unaffected by the diamagnetic frequency in the collisionless regime, while it is strongly modified in the semicollisional and collisional regimes. The widths of the tearing layers are broadened in all three regimes. Two-fluid equations in a cylindrical plasma were also used to investigate these effects,[12,13] and the results qualitatively agreed with the kinetic results in the collisional regime when the temperature gradient was neglected. Later, the temperature gradient was considered in the fluid theory, and it was noted that neglecting electron-electron collisions in kinetic theories may lead to overestimation of the relative importance of the driving source of the temperature gradient. The effects of perpendicular electron heat transport[14] and nonlinear effects[15–17] were also studied and found to significantly change the behavior of drift-tearing modes.

Many simulations of tearing modes and drift-tearing modes have been performed. A hybrid model consisting of a resistive MHD background plasma and kinetic energetic particles was used to investigate the kinetic effects on resistive tearing modes using the M3D code[18] and NIMROD.[19] Using the Gyrokinetic Toroidal Code (GTC)[20–22] and VirtEx,[23] a linear simulation of a resistive tearing mode in a cylindrical geometry in the fluid limit has been conducted to verify the relationship between the growth rate and the resistivity derived through theoretical analysis. A linear gyrokinetic model in a toroidal geometry implemented in the GKW code[24] and a gyrokinetic-ion drift-kinetic-electron model in a cylindrical geometry implemented in the GEM code[25] have been utilized to study collisionless and semicollisional drift-tearing modes. Fluid simulations[14,17,26,27] have also been performed using reduced two-fluid equations to investigate the thermal transport effects and nonlinear effects on a collisional drift-tearing mode.

In previous work, a physical model for tearing mode simulations using GTC has been established by beginning with the gyrokinetic equations in an inhomogeneous magnetic field,[21] building up a fluid model for electrons by integrating the electron gyrokinetic equation in the drift-kinetic limit,[28] and introducing a parallel electron force balance equation to capture the tearing mode mechanism with $\delta E_\parallel (k_\parallel = 0) \neq 0$,[23] thus forming a hybrid model of gyrokinetic ions and fluid electrons. Finally, the two-component equations are reduced to MHD equations in the linear long-wavelength limit by neglecting ion finite Larmor radius (FLR) effects. In this paper, a cross field pressure gradient term is considered in the parallel electron force balance equation to derive a drift-tearing mode model for the first time on the GTC platform. Our reduced MHD model for drift-tearing mode

simulations is different from the previous two-fluid simulation model in several respects. The vorticity equation is not needed in our system, but the gyrokinetic Poisson equation is included. We theoretically derive the dispersion relation of a drift-tearing mode based on our MHD model in order to benchmark the simulation results.

Linear simulations of resistive tearing modes and drift-tearing modes with $m = 2$ and $n = 1$ in a cylindrical geometry are performed using GTC with the gyro-MHD equations. The simulations of resistive tearing modes are first verified by a scan of $\beta_e$ values, which shows good agreement with the theoretical predictions and reflects the effects of pressure perturbations. Then, a diamagnetic frequency scan is performed for the drift-tearing modes to verify the theoretically predicted dispersion relation. The scaling relation between the growth rate and the diamagnetic frequency shows quantitative agreement with the theoretical results when the resistivity is relatively small. However, we observe an obvious deviation when the resistivity is large; this deviation arises because the constant-$\psi$ assumption results in a larger error for a wider tearing layer.

This paper is organized as follows: in Sec. II, we describe the physics model used to simulate drift-tearing modes in GTC, and we derive the dispersion relation for a drift-tearing mode. In Sec. III, the simulation parameters are introduced. In Sec. IV, the simulation results for resistive tearing modes are presented. In Sec. V, the simulation results for drift-tearing modes are reported. In Sec. VI, a conclusion and prospects for future research are presented.

## II. PHYSICAL MODEL

Through the work of previous researchers, a model for simulating resistive tearing modes in GTC has been established. Starting from a previous electromagnetic gyrokinetic model in a toroidal geometry,[21] a parallel electron force balance equation was introduced for the simulation of tearing modes.[23] Thus, a hybrid model with gyrokinetic equations for ions and fluid equations for electrons was derived. Finally, gyro-MHD equations were derived by reducing the two-component equations in the linear long-wavelength limit.

Based on this previous simulation model for resistive tearing modes, we introduce a cross field pressure gradient term into the parallel electron force balance equation to capture the effects of diamagnetic drift on tearing modes, which lead to the emergence of drift-tearing modes, for the first time. Since a fluid simulation is the first step of our work, the gyro-MHD equations are used as the simulation model. The kinetic effects on tearing modes will be a subject of our future research. Moreover, we analytically solve the MHD equations in a cylindrical geometry using the boundary layer method for comparison to the simulation results, and the dispersion relation for a drift-tearing mode is derived.

### A. Gyrokinetic equations

The original model is based on a gyrokinetic equation in an inhomogeneous magnetic field with the gyrocenter coordinates $(\mathbf{X}, \mu, v_\parallel)$,

$$\frac{d}{dt} f_\alpha(\mathbf{X}, \mu, v_\parallel, t) \equiv \left[ \frac{\partial}{\partial t} + \dot{\mathbf{X}} \cdot \nabla + \dot{v}_\parallel \frac{\partial}{\partial v_\parallel} \right] f_\alpha = 0. \quad (1)$$

Here, $\mathbf{X}$ is the position of the gyrocenter, $\mu$ is the magnetic moment, and $v_\parallel$ is the particle velocity along the magnetic field. The collision term is omitted here to consider a collisionless plasma. The index $\alpha$

represents different particle species ($i$ for ions or $e$ for electrons). The velocity of the gyrocenter consists of both parallel and perpendicular components; the perpendicular component includes the $E \times B$ drift, magnetic curvature drift, and magnetic gradient drift velocities,

$$\dot{\mathbf{X}} = v_\parallel \frac{\mathbf{B}}{B_0} + \mathbf{v}_E + \mathbf{v}_c + \mathbf{v}_g$$

$$= v_\parallel \frac{\mathbf{B}}{B_0} + \frac{c\mathbf{b}_0 \times \nabla\phi}{B_0} + \frac{v_\parallel^2}{\Omega_\alpha} \nabla \times \mathbf{b}_0 + \frac{\mu}{m_\alpha \Omega_\alpha} \mathbf{b}_0 \times \nabla B_0, \quad (2)$$

and the parallel acceleration is

$$\dot{v}_\parallel = -\frac{1}{m_\alpha} \frac{\mathbf{B}^*}{B_0} \cdot (\mu \nabla B_0 + Z_\alpha \nabla\phi) - \frac{Z_\alpha}{m_\alpha c} \frac{\partial A_\parallel}{\partial t}. \quad (3)$$

Here, $Z_\alpha$ and $m_\alpha$ denote the particle charge and mass, respectively; $\phi$ and $A_\parallel$ denote the electrostatic potential and parallel vector potential, respectively; $\Omega_\alpha$ is the gyrofrequency; $\mathbf{B} \equiv \mathbf{B}_0 + \boldsymbol{\delta B}$ is the total magnetic field, with $\mathbf{B}_0 \equiv B_0 \mathbf{b}_0$; and

$$\mathbf{B}^* = \mathbf{B}_0^* + \boldsymbol{\delta B} = \mathbf{B}_0 + \frac{B_0 v_\parallel}{\Omega_\alpha} \nabla \times \mathbf{b}_0 + \boldsymbol{\delta B}, \quad (4)$$

where $\boldsymbol{\delta B} = \nabla \times \delta A_\parallel \mathbf{b}_0$, which is obtained by excluding the compressional component of the perturbed magnetic field. The perturbative $\delta f$ method is utilized to rewrite the perturbed part of Eq. (1) for ions in order to minimize the discrete particle noise,

$$\frac{d\omega_i}{dt} = (1 - \omega_i)\left[ -\left(v_\parallel \frac{\delta\mathbf{B}}{B_0} + \mathbf{v}_E\right) \cdot \frac{\nabla f_{0i}}{f_{0i}} \right.$$
$$\left. + \left(\mu \frac{\delta\mathbf{B}}{B_0} \cdot \nabla B_0 + Z_i \frac{\mathbf{B}^*}{B_0} \cdot \nabla\delta\phi + \frac{Z_i}{c}\frac{\partial \delta A_\parallel}{\partial t}\right) \times \frac{1}{m_i} \frac{1}{f_{0i}} \frac{\partial f_{0i}}{\partial v_\parallel} \right], \quad (5)$$

where $\omega_i \equiv \delta f_i / f_i$ is the particle weight for ions. The perturbed electrostatic potential and parallel vector potential are derived via the gyrokinetic Poisson equation and the gyrokinetic Ampère's law,

$$(\delta\phi - \delta\tilde{\phi}) \frac{4\pi Z_i^2 n_{0i}}{T_i} = 4\pi(Z_i \delta\bar{n}_i - e\delta n_e), \quad (6)$$

$$n_{0e} e \delta u_{\parallel e} = \frac{c}{4\pi} \nabla_\perp^2 \delta A_\parallel + n_{0i} Z_i \delta u_{\parallel i}. \quad (7)$$

Here, $\delta\tilde{\phi}$ is the second gyroaveraged potential,[20] the left side of Eq. (6) represents the ion polarization density, $\delta\bar{n}_i$ is the gyroaveraged perturbed ion density, and $\delta u_{\parallel i}$ and $\delta u_{\parallel e}$ are the perturbed parallel velocities of ions and electrons, respectively.

## B. Fluid model for electrons

Since we adopt a relatively large resistivity, the electron gyroradius is much smaller than the width of the tearing layer. The perturbed electron continuity equation is derived by integrating Eq. (1) in the drift-kinetic limit while retaining only the linear perturbation terms,

$$\frac{\partial \delta n_e}{\partial t} + B_0 \mathbf{b}_0 \cdot \nabla\left(\frac{n_{0e}\delta u_{\parallel e}}{B_0}\right) + B_0 \mathbf{v}_E \cdot \nabla\left(\frac{n_{0e}}{B_0}\right)$$
$$- n_{0e}(\delta\mathbf{v}_* + \mathbf{v}_E) \cdot \frac{\nabla B_0}{B_0} + \delta\mathbf{B} \cdot \nabla\left(\frac{n_{0e}u_{\parallel 0e}}{B_0}\right)$$
$$+ \frac{c\nabla \times \mathbf{B}_0}{B_0^2} \cdot (-\nabla\delta p_{\parallel e} + n_{0e}\nabla\delta\phi) = 0, \quad (8)$$

where $\delta\mathbf{v}_* = \mathbf{b}_0 \times \nabla(\delta p_{\parallel e} + \delta p_{\perp e})/(n_{0e}m_e\Omega_e)$ is the perturbed electron diamagnetic drift, $\delta p_{\parallel e} = \int d\mathbf{v} m v_\parallel^2 \delta f_e$, $\delta p_{\perp e} = \int d\mathbf{v} \mu B_0 \delta f_e$, and $\Omega_e$ is the electron cyclotron frequency. Note that the fifth term, induced by the gradient of the parallel equilibrium flow, is the driving source of the classical tearing mode, and the sixth term, associated with a finite $\nabla \times \mathbf{B}_0$, is also important in our case. Nonlinear terms are ignored in this paper for simplicity; however, nonlinear effects will be studied in the future. The following parallel electron force balance equation is introduced to close the field equations:

$$\delta E_\parallel = -\eta e n_{0e}(\delta u_{\parallel i} - \delta u_{\parallel e}) - \frac{1}{en_{0e}} \mathbf{b}_0 \cdot \nabla\delta p_e - \frac{1}{en_{0e}} \frac{\delta\mathbf{B}}{B_0} \cdot \nabla p_{0e}, \quad (9)$$

where $\eta = \nu_{ei}m_e/(e^2 n_{0e})$ is the plasma resistivity, $\nu_{ei}$ is the electron-ion collision frequency, $\delta p_e = \delta p_{\parallel e} = \delta p_{\perp e}$ with the application of adiabatic approximation, and $p_{0e}$ is the equilibrium electron pressure. Together with the relation $\delta E_\parallel = -\mathbf{b}_0 \cdot \nabla\delta\phi - (1/c)(\partial \delta A_\parallel/\partial t)$, this equation can be used to derive a simulation form for calculating the perturbed parallel vector potential as follows:

$$\frac{\partial \delta A_\parallel}{\partial t} = -c\mathbf{b}_0 \cdot \nabla\delta\phi + c\eta e n_{0e}(\delta u_{\parallel i} - \delta u_{\parallel e})$$
$$+ \frac{c}{en_{0e}} \mathbf{b}_0 \cdot \nabla\delta p_e + \frac{c}{en_{0e}} \frac{\delta\mathbf{B}}{B_0} \cdot \nabla p_{0e}. \quad (10)$$

Thus far, Eqs. (2)–(8) and (10) form a closed system with gyrokinetic ions and fluid electrons for tearing mode simulations.

## C. Reduction to the MHD limit

In the linear long-wavelength limit, the two-component equations reduce to MHD equations. We assume that ions and electrons have the same charge, $Z_i = -Z_e = e$, and that equilibrium quasineutrality is enforced, $n_{0i} = n_{0e} = n_0$. The notations $\delta n = \delta n_i - \delta n_e$ and $\delta u_\parallel = \delta u_{\parallel i} - \delta u_{\parallel e}$ are defined for simplicity. The Poisson equation given in Eq. (6) becomes

$$\frac{c^2}{4\pi e v_A^2} \nabla_\perp^2 \delta\phi = \delta n. \quad (11)$$

Ampère's law in Eq. (7) is similarly rewritten as

$$n_0 e \delta u_\parallel = \frac{c}{4\pi} \nabla_\perp^2 \delta A_\parallel. \quad (12)$$

The ion continuity equation is derived by integrating the gyrokinetic equation given in Eq. (1) in the linear limit. In particular, terms associated with ion FLR effects are ignored here because the ion gyroradius is also smaller than the width of the current layer in our case. Then, subtracting the ion continuity equation from the electron continuity equation results in the MHD continuity equation, as follows:

$$\frac{\partial \delta n}{\partial t} + B_0 \mathbf{b}_0 \cdot \nabla\left(\frac{n_0 \delta u_\parallel}{B_0}\right) - n_0 \mathbf{v}_* \cdot \frac{\nabla B_0}{B_0}$$
$$+ \delta\mathbf{B} \cdot \nabla \frac{n_0 u_{\parallel 0}}{B_0} - \frac{c\nabla \times \mathbf{B}_0}{B_0^2} \cdot \nabla\delta p_\parallel = 0. \quad (13)$$

Similarly, the parallel generalized Ohm's law can be obtained from the perturbed ion and electron momentum equations in the parallel direction,

$$\delta E_\parallel = -\eta e n_0 \delta u_\parallel - \frac{1}{e n_0} \nabla_\parallel \delta p - \frac{1}{e n_0} \frac{\delta \mathbf{B}}{B_0} \cdot \nabla p_0, \quad (14)$$

and Eq. (10) becomes

$$\frac{\partial \delta A_\parallel}{\partial t} = -c \mathbf{b}_0 \cdot \nabla \delta \phi + c \eta e n_{0e} \delta u_\parallel$$
$$+ \frac{c}{e n_0} \mathbf{b}_0 \cdot \nabla \delta p + \frac{c}{e n_0} \frac{\delta \mathbf{B}}{B_0} \cdot \nabla p_0. \quad (15)$$

Equations (11)–(13) and (15) can be used for linear fluid simulations of resistive tearing modes and drift-tearing modes.

## D. The solution of the MHD equations

For comparison with the simulation results, we analytically solve the MHD equations in a cylindrical geometry ($\nabla B_0 = 0$). The MHD equations are simplified to the following form:

$$\frac{\partial \delta n}{\partial t} + n_0 \nabla_\parallel \delta u_\parallel + \frac{\delta \mathbf{B}}{e B_0} \cdot \nabla J_{\parallel 0} = 0, \quad (16)$$

$$\delta u_\parallel = \frac{c}{4 \pi n_0 e} \nabla_\perp^2 \delta A_\parallel, \quad (17)$$

$$\frac{c^2}{v_A^2} \nabla_\perp^2 \delta \phi = 4 \pi e \delta n, \quad (18)$$

$$\frac{1}{c} \frac{\partial \delta A_\parallel}{\partial t} + \nabla_\parallel \delta \phi = \eta \frac{c}{4\pi} \nabla_\perp^2 \delta A_\parallel + \frac{1}{e n_0} \nabla_\parallel \delta p + \frac{1}{e n_0} \frac{\delta \mathbf{B}}{B_0} \cdot \nabla p_0. \quad (19)$$

To analyze the linear drift-tearing mode, the perturbed quantity $h(\mathbf{x}, t)$ is assumed to vary as $h_0(r) + \delta h_{m,n}(r) \exp[im\theta + inz - i\omega t]$ in cylindrical coordinates. $\delta h_{m,n}(r)$ satisfies the following boundary conditions: $\delta h_{m,n}(0) = 0$ and $\delta h_{m,n}(1) = 0$. The compressional component of the magnetic field perturbation is excluded by assuming $\delta B_\parallel = 0$. The isothermal model is used, i.e., $T = const$, $p = nT$. Then, we adopt the substitutions $\partial / \partial t \to -i\omega$ and $\mathbf{b}_0 \cdot \nabla \to i k_\parallel$ from linear normal mode theory, and the equations become

$$-i\omega \delta n + n_0 i k_\parallel \delta u_\parallel + \frac{i k_\theta \delta A_\parallel}{e B_0} J'_{\parallel 0} = 0, \quad (20)$$

$$\delta u_\parallel = \frac{c}{4 \pi n_0 e} (\delta A_\parallel'' - k_\theta^2 \delta A_\parallel), \quad (21)$$

$$\frac{c^2}{v_A^2} (\delta \phi'' - k_\theta^2 \delta \phi) = 4 \pi e \delta n, \quad (22)$$

$$\frac{-i\omega}{c} \delta A_\parallel + i k_\parallel \delta \phi = \eta \frac{c}{4\pi} (\delta A_\parallel'' - k_\theta^2 \delta A_\parallel)$$
$$+ \frac{1}{e n_0} i k_\parallel T_0 \delta n + \frac{i k_\theta T_0}{e B_0} \frac{n_0'}{n_0} \delta A_\parallel, \quad (23)$$

where a prime symbol indicates a radial derivative and $k_\parallel$ and $k_\theta$ are the parallel and perpendicular wave numbers, respectively. Equations (20)–(23) yield the following coupled equations for $\delta \phi$ and $\delta A_\parallel$:

$$(\delta A_\parallel'' - k_\theta^2 \delta A_\parallel) + i(\omega - \omega^*) \frac{4\pi}{c^2 \eta} \delta A_\parallel = i k_\parallel \frac{4\pi}{c\eta} \frac{\omega - \omega^*}{\omega} \delta \phi, \quad (24)$$

$$\frac{c^2}{v_A^2} \frac{\omega}{4\pi e} (\delta \phi'' - k_\theta^2 \delta \phi) = \frac{k_\parallel c}{4\pi e} (\delta A_\parallel'' - k_\theta^2 \delta A_\parallel) + \frac{k_\theta J'_{\parallel 0}}{e B_0} \delta A_\parallel, \quad (25)$$

where $\omega^* = -(k_\theta T_0 / e B_0)(n_0' / n_0)$ is the diamagnetic frequency. We solve these equations in the singular layer (internal region,

$r - r_s < r_c \ll 1$). We assume that $\delta A_\parallel = const$ (equivalent to the constant-$\psi$ approximation) in a narrow layer and that

$$\delta A_\parallel'' \gg k_\theta^2 \delta A_\parallel, \quad (26)$$

$$\delta \phi'' \gg k_\theta^2 \delta \phi. \quad (27)$$

Equations (24) and (25) become

$$\delta A_\parallel'' + i(\omega - \omega^*) \frac{4\pi}{c^2 \eta} \delta A_\parallel = i k_\parallel \frac{4\pi}{c\eta} \frac{\omega - \omega^*}{\omega} \delta \phi, \quad (28)$$

$$\frac{c^2}{v_A^2} \frac{i\omega}{4\pi e} \delta \phi'' = \frac{i k_\parallel c}{4\pi e} \delta A_\parallel'' - \frac{i k_\theta J'_{\parallel 0}}{B_0} \delta A_\parallel. \quad (29)$$

We substitute Eqs. (28) into (29) and define $\delta A_\parallel = \delta A_\parallel^{(0)} = const$, $k_\parallel = k_\theta(r - r_s)/l_s$, $l_s = B_0/(\partial B_{\theta 0}/\partial r)$, and $J'_{\parallel 0} \sim B_\theta'' \sim 0$, thus obtaining

$$i\omega \frac{c^2}{v_A^2} \delta \phi'' + \frac{4\pi}{\eta} \frac{k_\theta^2}{l_s^2} (r - r_s)^2 \frac{\omega - \omega^*}{\omega} \delta \phi$$
$$= \frac{4\pi}{c\eta} (\omega - \omega^*) \frac{k_\theta}{l_s} (r - r_s) \delta A_\parallel^{(0)}, \quad (30)$$

with the definitions

$$\frac{k_\theta}{l_s}(r - r_s) = \left( \frac{c^2 \eta k_\theta^2}{i 4\pi v_A^2 l_s^2} \right)^{\frac{1}{4}} \left( \frac{\omega^2}{\omega - \omega^*} \right)^{\frac{1}{4}} z, \quad (31)$$

$$\delta \phi(r) = -\left( \frac{i 4\pi v_A^2 l_s^2}{c^2 \eta k_\theta^2} \right)^{\frac{1}{4}} \left( \frac{\omega - \omega^*}{\omega^2} \right)^{\frac{1}{4}} c\omega \delta A_\parallel^{(0)} \chi(z), \quad (32)$$

Equation (30) becomes

$$\chi''(z) - z^2 \chi(z) = z. \quad (33)$$

The solution to this equation is

$$\chi(z) = -\frac{z}{2} \int_0^1 -\frac{\exp(-\mu z^2/2)}{(1 - \mu^2)^{1/4}} d\mu. \quad (34)$$

Therefore, the solutions for $\delta \phi$ and $\delta A_\parallel$ in the internal region are

$$\delta \phi = -\left( \frac{i 4\pi v_A^2 l_s^2}{c^2 \eta k_\theta^2} \right)^{\frac{1}{4}} \left( \frac{\omega - \omega^*}{\omega^2} \right)^{\frac{1}{4}} c\omega \delta A_\parallel^{(0)} \chi(z), \quad (35)$$

$$\delta A_\parallel = \delta A_\parallel^{(0)}. \quad (36)$$

Thus, we obtain

$$\Delta = \frac{1}{\delta A_\parallel^{(0)}} \int_{-\infty}^{\infty} \delta A_\parallel'' dr$$
$$= \frac{c\omega}{v_A^2} \frac{1}{\delta A_\parallel^{(0)}} \int_{-\infty}^{\infty} \frac{\delta \phi''}{k_\parallel} dr$$
$$= -\frac{c^2 \omega^2}{v_A^2} \left( \frac{i 4\pi v_A^2}{c^2 \eta} \right)^{\frac{3}{4}} \left( \frac{l_s}{k_\theta} \right)^{\frac{1}{2}} \left( \frac{\omega - \omega^*}{\omega^2} \right)^{\frac{3}{4}} \int_{-\infty}^{\infty} \frac{\chi''(z)}{z} dz, \quad (37)$$
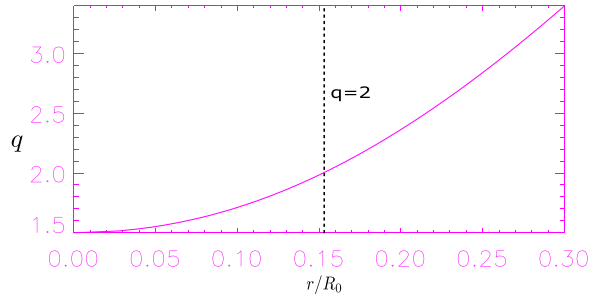
**FIG. 1.** Radial safety factor profile, $q = 1.5 + 1.2\psi/\psi_w + 0.7(\psi/\psi_w)^2$. The dashed line shows the position of the $q = 2$ rational surface at $r/R_0 = 0.152$.
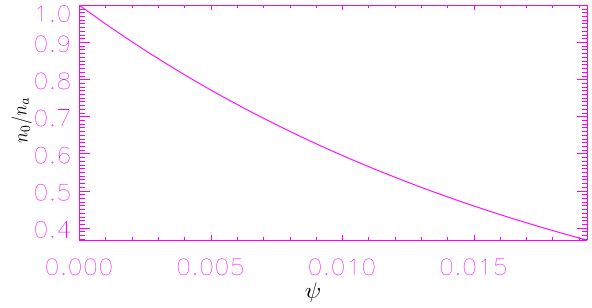


**FIG. 2.** Radial profile of the equilibrium density, $n_0 = n_a e^{(-\psi/\psi_w)}$, for the simulation of drift-tearing modes.

where $\int_{-\infty}^{\infty} \frac{\chi''(z)}{z} dz = \pi\Gamma(3/4)/\Gamma(1/4)$. The dispersion relation is derived by matching the expressions for the internal region and the outer region, $\Delta = \Delta'$,

$$\omega^2(\omega - \omega^*)^3 = i\gamma_c^5, \tag{38}$$

where $\gamma_c = (\Gamma(1/4)/\pi\Gamma(3/4))^{4/5}\Delta'^{4/5}(\eta/4\pi)^{3/5}(v_A k_\theta/cl_s)^{2/5}$. The limiting values of $\omega$ are

$$\omega = \begin{cases} \dfrac{3}{5}\omega^* + i\gamma_c, & \text{if } \omega^* \ll \gamma_c; \\[2mm] \omega^* + i\gamma_c\left(\dfrac{\gamma_c^2}{\omega^{*2}}\right)^{\frac{1}{3}}, & \text{if } \omega^* \gg \gamma_c. \end{cases} \tag{39}$$

This result is qualitatively consistent with Biskamp's theoretical derivation.[12] The differences mainly lie in the lack of $\omega_i^*$ and the
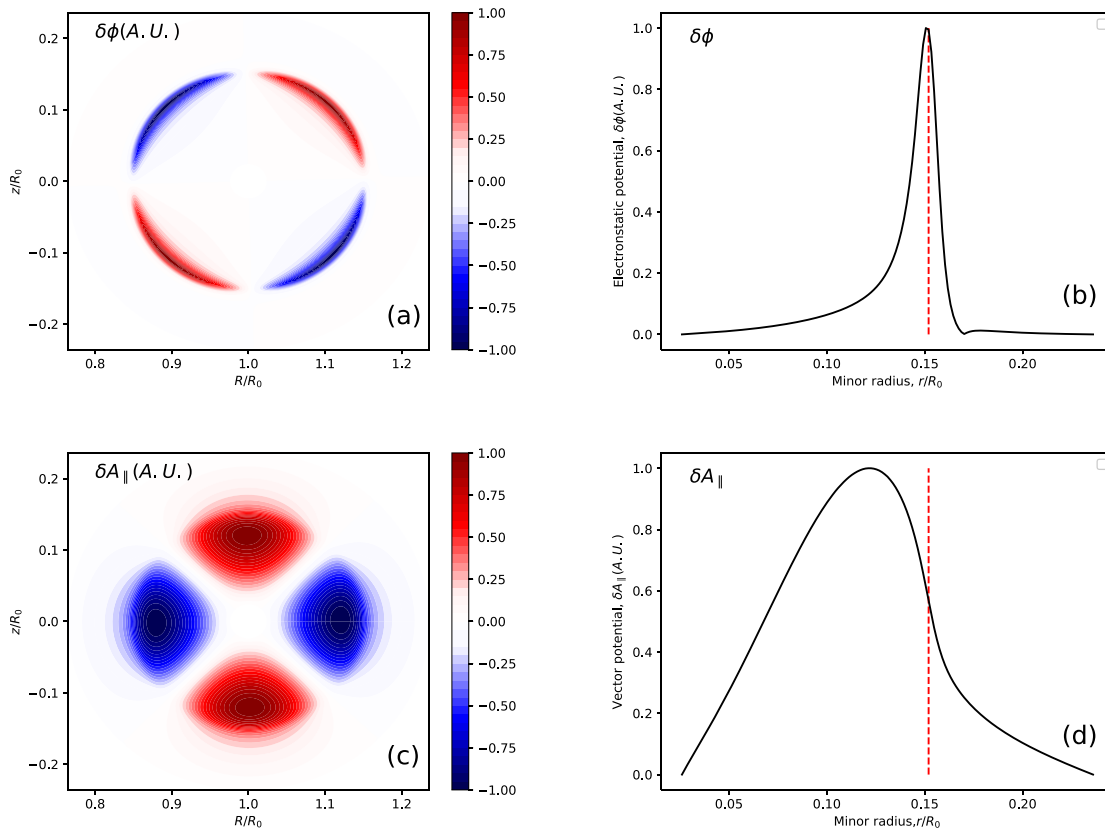


**FIG. 3.** Mode structure of the $(m, n) = (2, 1)$ resistive tearing mode on the poloidal plane and in the radial direction. Panels (a) and (c) show the contours of the perturbed electrostatic potential $\delta\phi$ and the perturbed vector potential $\delta A_\parallel$ on the poloidal cross section, respectively. Panels (b) and (d) show the radial profile of $\delta\phi$ and $\delta A_\parallel$, respectively. The red dashed lines in panels (b) and (d) indicate the position of the $q = 2$ rational surface.

coefficient of 1/2 before the imaginary part of $\omega$ in the $\omega^* \gg \gamma_c$ case, which result from neglecting the ion FLR effects and the ion viscosity term, respectively.

## III. SIMULATION SETUP

Both the $(m, n) = (1, 1)$ and $(2, 1)$ tearing modes are known to be important MHD instabilities in tokamak discharges. The $(1, 1)$ tearing modes are also called kink-tearing modes due to the strong coupling between the kink mode and the tearing mode and are distinct from the $m > 1$ tearing modes.[3] To eliminate the effects of kink coupling, our work focuses on the $(2, 1)$ modes. A safety factor profile of $q = 1.5 + 1.2\psi/\psi_w + 0.7(\psi/\psi_w)^2$ is used to contain the $q = 2$ rational surface in the simulation region, as shown in Fig. 1, where $\psi$ is the poloidal flux, $\psi = 0$ at the magnetic axis, and $\psi = \psi_w$ at the plasma boundary. The inverse aspect ratio is $\epsilon \equiv a/R = 0.3$, where $a$ and $R$ are the minor and major radii, respectively, of the tokamak device; the on-axis major radius is set to $R_0 = 1\,m$.

For the resistive tearing mode simulations, the equilibrium density and temperature are uniform, with the same values for electrons and ions: $n_{0e} = n_{0i}$ and $T_{0e} = T_{0i}$. The plasma resistivity is set to a constant value of $\eta = 1.8 \times 10^{-6}\,\Omega \cdot m$. For the case of showing the mode structure on the poloidal plane, the equilibrium density and temperature are $n_{0e} = 1.0 \times 10^{20}\,m^{-3}$ and $T_{0e} = 3\,keV$, respectively, and the magnetic field is $B_0 = 2\,T$, resulting in $\beta_e = 3\%$, where $\beta_e = 8\pi n_a T_{0e}/B_a^2$ is the plasma on-axis beta for electrons, with $n_a$ and $B_a$ denoting the on-axis equilibrium values. We choose a radial profile similar to the eigenmode structure as the initial perturbation of the vector potential to reduce the simulation time.

For the drift-tearing mode simulations, most of the simulation parameters are the same as those for the previous $(2, 1)$ resistive tearing mode case, except for the introduction of a nonuniform equilibrium density distribution of $n_0 = n_a e^{(-\psi/\psi_w)}$, as shown in Fig. 2, where $n_0 = n_{0e} = n_{0i}$ and $n_a$ is the equilibrium on-axis density. The
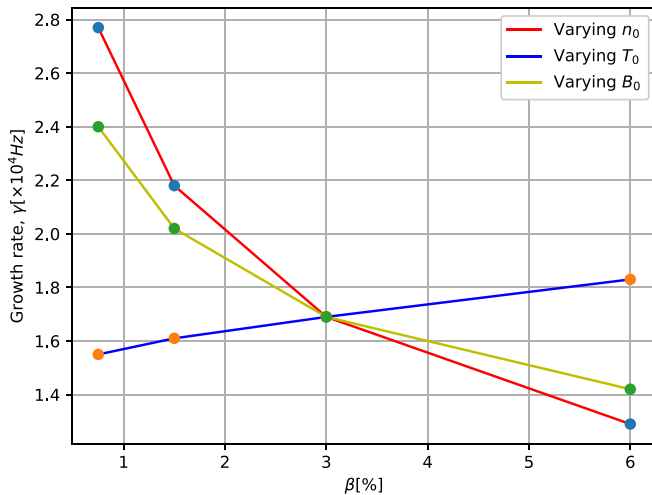


FIG. 5. Scaling relation between the growth rate of the (2,1) resistive tearing mode and the electron beta value when the equilibrium magnetic field is varied.



FIG. 4. Variations in the growth rate of the (2,1) resistive tearing mode with four different $\beta$ values: 0.75%, 1.5%, 3%, and 6%. The red line shows the results obtained when varying the density. The blue line shows the results obtained when varying the temperature. The yellow line shows the results obtained when varying the magnetic field.
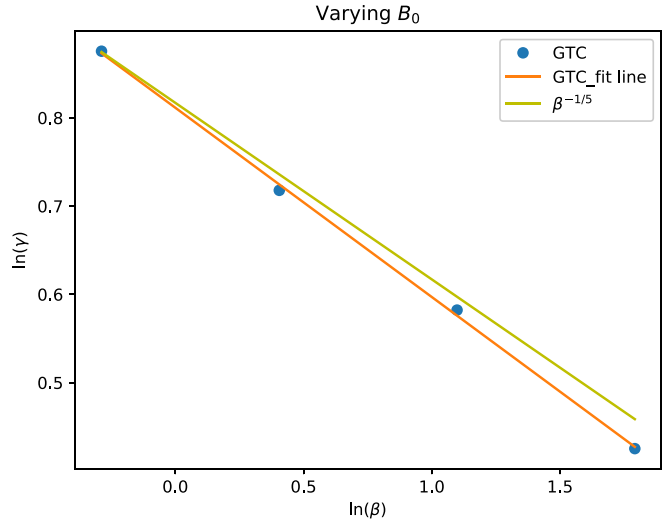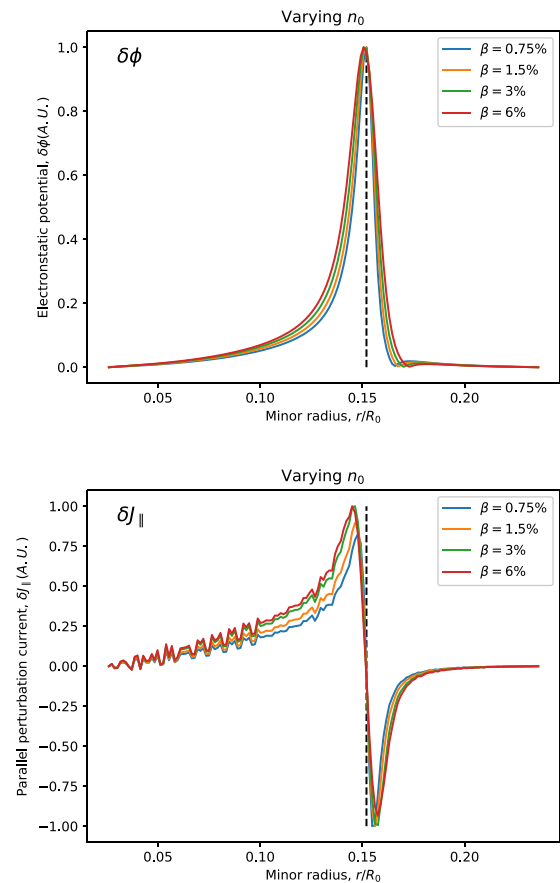


FIG. 6. The perturbed electrostatic potential and perturbed parallel current profiles with four different $\beta$ values (0.75%, 1.5%, 3%, and 6%) when the density is varied. The dashed line in each panel indicates the position of the $q = 2$ rational surface.

density on the $q = 2$ rational surface is set to $n_s = 1.0 \times 10^{20}$ m$^{-3}$. The equilibrium temperature is still treated as uniform.

## IV. SIMULATION OF RESISTIVE TEARING MODES

Linear simulations of resistive tearing modes are carried out to verify the capabilities of the code and benchmark the results against previous simulation work based on GTC.[22] For simplicity, the reduced MHD model is used, while ignoring the equilibrium pressure gradient, the kinetic effects of ions, and the effects of the toroidal geometry. The mode structure of the (2, 1) resistive tearing mode is shown in Fig. 3, with the contours of $\delta\phi$ and $\delta A_\parallel$ on the poloidal cross section and the corresponding radial profile at $\theta = 0$. All curves are normalized with respect to their maximum absolute values. In the simulations, only mode numbers of $m = 2$ and $n = 1$ are retained; other modes are filtered out via Fourier transformation.

The contour plots in Figs. 3(a) and 3(c) show the symmetry in the radial direction in a simulation with a cylindrical geometry. The radial profile plot in Fig. 3(b) shows a steep variation in the perturbed electrostatic potential that is concentrated near the $q = 2$ rational surface, while the perturbed parallel vector potential in Fig. 3(d) is globally distributed in the radial direction. The nonzero value of $\delta A_\parallel$ on the

$q = 2$ rational surface corresponds to the perturbed parallel current due to the finite resistivity, $\delta j_\parallel \sim \nabla_\perp^2 \delta A_\parallel$. For the specific parameters given previously, the pure tearing eigenmode has a growth rate of $\gamma = 1.71 \times 10^4$ Hz.

Since the scaling relation between the growth rate and the resistivity has been benchmarked against theory before,[22] we perform a scan of various plasma beta values to obtain the growth rate and mode structure for further verification. The relative trend of variation between the beta value and the tearing mode growth rate can help us to study the drift-tearing mode, which will be discussed in the next section. The magnetic reconnection caused by the tearing mode is driven by the magnetic energy difference between the initial and final states. The time scale of mode growth is determined by a combination of the resistive diffusion time, which is related to the diffusion of the magnetic field lines through the plasma, and the Alfvén time, which is related to the ideal plasma response. For a linear collisional tearing mode, theory predicts[4] that the growth rate should follow the relation $\gamma \propto \tau_R^{-3/5} \tau_A^{-2/5}$, where $\tau_R = a^2/\eta$ is the resistive diffusion time, $\tau_A = (n_0 M)^{1/2} a^2 m / B_{\theta 0} R$ is the Alfvén time, $M = m_i m_e / (m_i + m_e)$ is the reduced mass, and $B_{\theta 0}$ is the equilibrium poloidal magnetic field, which satisfies $B_{\theta 0} \propto B_0$ for a fixed $q$ value. Thus, we can derive the
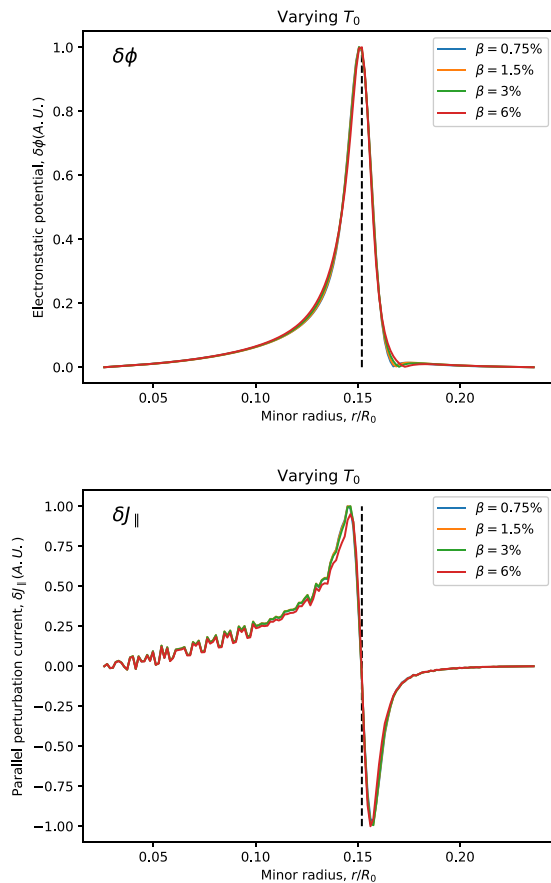


**FIG. 7.** The perturbed electrostatic potential and perturbed parallel current profiles with four different $\beta$ values (0.75%, 1.5%, 3%, and 6%) when the temperature is varied.
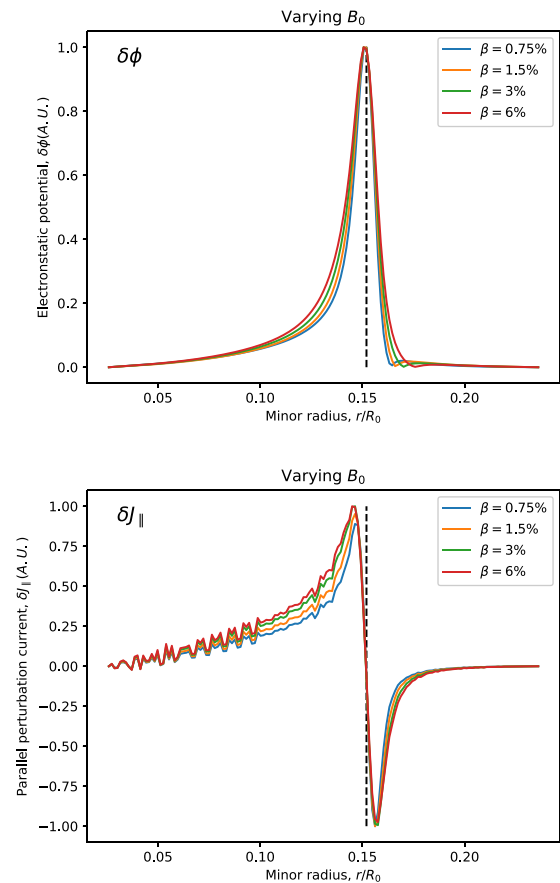
**FIG. 8.** The perturbed electrostatic potential and perturbed parallel current profiles with four different $\beta$ values (0.75%, 1.5%, 3%, and 6%) when the magnetic field is varied.

relation $\gamma \propto n_0^{-1/5} B_0^{2/5}$, indicating that the growth rate $\gamma$ depends on $\beta^{-1/5}$ for a fixed $T_0$.

To benchmark the simulation results in GTC, the relationship between the growth rate and the electron beta, $\beta$, is calculated. We scan four different $\beta$ values: 0.75%, 1.5%, 3%, and 6%. There are three parameters we can vary to obtain different $\beta$ values, namely, the equilibrium density $n_0$, the temperature $T_0$, and the magnetic field $B_0$, thus leading to different and even opposite results. As shown in Fig. 4, when the density and magnetic field are varied, the growth rate decreases with an increase in $\beta$, whereas when the temperature is varied, the growth rate slightly increases with an increase in $\beta$.

These differences arise from the influence of the perturbed pressure in Ohm's law, that is, the third term on the right-hand side of Eq. (14), $(1/en_0)\nabla_\parallel \delta p$. From the expression for this term, we can see that the driving force from the perturbed pressure term increases as the equilibrium temperature increases and as the equilibrium density decreases.

In Fig. 5, the simulated and predicted scaling relations are compared by taking the logarithms of the growth rates and electron beta values for the "Varying $B_0$" curve. The slope of the fitted line is –0.214, which agrees well with the theoretically predicted value of $--1/5$.

Theory also predicts that the width of the tearing layer should be $\Delta_c \simeq (\nu_{ei}/\gamma_k)^{2/5} \rho_i^{2/5} \Delta_k^{3/5}$ for a linear collisional tearing mode,[10] where

$\gamma_k \approx (v_{te}/l_s)(k_0 a)^{-2}$ and $\Delta_k \approx (k_0 a)^{-1}$ denote the growth rate and layer width, respectively, of the collisionless tearing mode; and $k_0^{-1} = c/\omega_{pe}$ is the collisionless skin depth. Through some standard analysis, we derive the dependencies $\Delta_k \sim k_0^{-1} \sim n_0$, $\gamma_k \sim v_{te}k_0^{-2} \sim T_0^{1/2}n_0$, and $\rho_i \sim T_0^{1/2}B_0^{-1}$; thus, the width of the collisional tearing layer obeys the following relation: $\Delta_c \sim \gamma_k^{-2/5} \rho_i^{2/5} \Delta_k^{3/5} \sim n_0 B_0^{-2/5}$.

Since precisely measuring the width of the tearing layer is difficult, we present only a qualitative comparison here. Figures 6–8 show the radial mode profiles for different $\beta$ values when the density, temperature, and magnetic field, respectively, are varied. The changes in the width of the tearing layer are qualitatively consistent with the linear collisional theory of tearing modes, i.e., the width of the tearing layer increases with an increase in $n_0$, decreases with an increase in $B_0$, and changes slightly with different values of $T_0$.

## V. SIMULATION OF DRIFT-TEARING MODES

In this section, the effects of the equilibrium pressure gradient on the resistive tearing instability are investigated. The equilibrium pressure gradient can affect the tearing modes in both the inner and outer regions, and the coupling of drift modes to tearing modes results in so-called drift-tearing modes, which will lead to significant changes in the mode structure and dispersion relation.
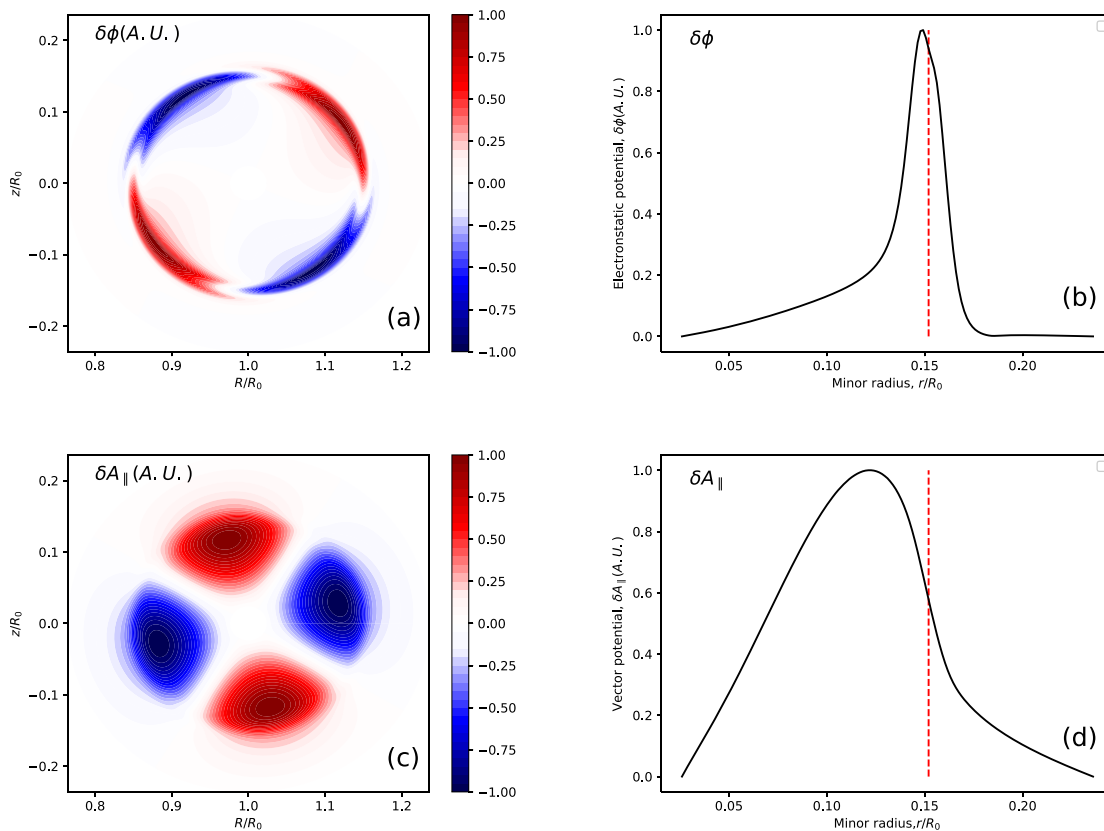


**FIG. 9.** Mode structure of the (2,1) drift-tearing mode on the poloidal plane and in the radial direction. Panels (a) and (c) show the contours of the perturbed electrostatic potential $\delta\phi$ and the perturbed vector potential $\delta A_\parallel$ on the poloidal cross section, respectively. Panels (b) and (d) show the radial profile of $\delta\phi$ and $\delta A_\parallel$, respectively. The red dashed lines in panels (b) and (d) indicate the position of the $q = 2$ rational surface.

The mode structure of the (2,1) drift-tearing mode is shown in Fig. 9, with the contours of $\delta\phi$ and $\delta A_\parallel$ on the poloidal cross section and the corresponding radial profile at $\theta = 0$. Mode number filtering is again applied to keep only the (2,1) mode. The contours of $\delta\phi$ and $\delta A_\parallel$ in Figs. 9(a) and 9(c) rotate along the poloidal direction due to the diamagnetic drift motion of the electrons, with a rotation frequency equal to the electron diamagnetic frequency. Notably, the poloidal mode structure of $\delta\phi$ in Fig. 9(a) also shows radial symmetry breaking relative to the resistive tearing mode case in Fig. 3(a). This symmetry breaking is due to the effects of radial variations of the pressure gradient; thus, the radial mode structure is also slightly deformed near the $q = 2$ rational surface, as shown in Fig. 9(b).

The radial profiles of the perturbed electrostatic potential and the perturbed parallel current for the resistive tearing mode and the drift-tearing mode are compared in Fig. 10, which shows that the effects of diamagnetic drift lead to broadening of the radial mode width and the current layer.

For a linear drift-tearing mode, the theoretically predicted width of the current layer is $\Delta \simeq (\omega^*/\gamma_c)^{2/3}\Delta_c$, where $\gamma_c$ and $\Delta_c$ are the growth rate and layer width, respectively, of the corresponding



**FIG. 11.** Scaling relation between the growth rate $\gamma$ of the (2,1) drift-tearing mode and the diamagnetic frequency $\omega*$. The straight yellow line, with a slope equal to $-2/3$, represents the theoretically predicted scaling relation; the blue points are the sample points when $\eta = 1.8 \times 10^{-6}\,\Omega \cdot m$, and the yellow points are the sample points when $\eta = 4.5 \times 10^{-7}\,\Omega \cdot m$.

collisional resistive tearing mode. The diamagnetic drift causes the current layer to broaden when $\omega^* > \gamma_c$. For our chosen simulation parameters, the diamagnetic frequency is calculated to be $\omega^* = 3.86\gamma_c$. Thus, the change in the mode width is consistent with theory.

As shown in Fig. 11, we scan different values of the diamagnetic frequency by varying the equilibrium density gradient to verify the theoretically predicted scaling relation between the growth rate and the diamagnetic frequency, i.e., $\gamma \sim \omega^{*-2/3}$; note that all values are plotted as their logarithms. Since previous simulation results presented in Fig. 4 show that the tearing mode growth rate decreases with increasing density when the gradient of the density is fixed at zero, we fix the local equilibrium density on the $q = 2$ rational surface here to ensure that the density gradient is the only variable. First, we choose a relatively large resistivity of $\eta = 1.8 \times 10^{-6}\,\Omega \cdot m$ (blue points), for which the sampled points deviate from the theoretically predicted straight line with a slope of $-2/3$ as the diamagnetic frequency increases. Then, we consider a smaller resistivity of $\eta = 4.5 \times 10^{-7}\,\Omega \cdot m$ (yellow points), for which the sampled points essentially coincide with the theoretically predicted line.

We know that the width of the tearing layer is related to the resistivity as follows: $\Delta \sim \eta^{2/5}$. When the resistivity is sufficiently large, the error introduced by the constant-$\psi$ assumption cannot be ignored. To gain a deeper understanding of this phenomenon, the widths of the tearing layer in the two different resistivity cases are compared in Fig. 12, where the half-width of the perturbed current profile is treated as the width of the tearing layer. Since a narrow current layer is the main restriction of the constant-$\psi$ assumption, this assumption obviously introduces larger error for a larger resistivity and a wider layer.

## VI. CONCLUSIONS

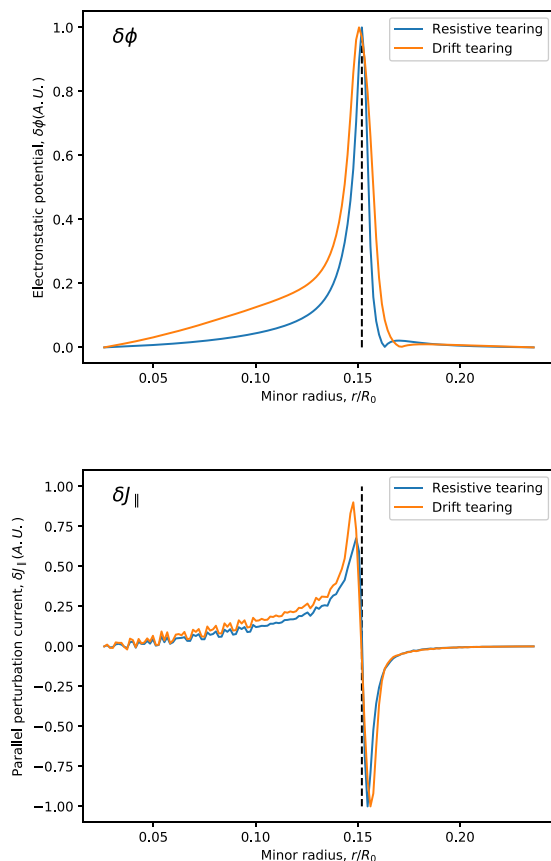Based on a previously developed simulation model for resistive tearing modes on the GTC platform, we introduce a cross field



**FIG. 10.** Comparison of the radial profiles of the perturbed electrostatic potential $\delta\phi$ and the perturbed parallel current $\delta J_\parallel$ between the resistive tearing mode and the drift-tearing mode. The blue lines represent the results for the resistive tearing mode, and the yellow lines represent the results for the drift-tearing mode. The dashed line in each panel indicates the position of the $q = 2$ rational surface.
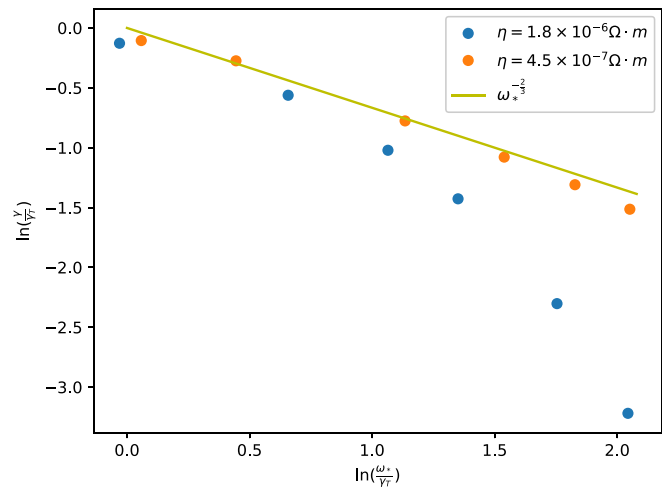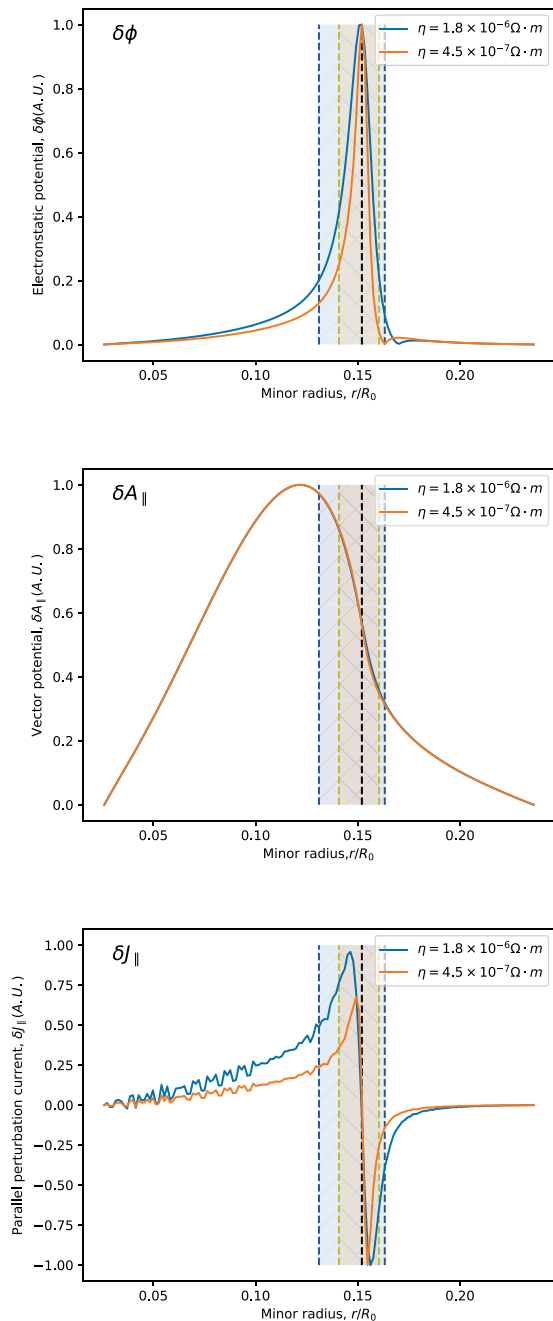
**FIG. 12.** The locations of the tearing layer in the radial profiles of the perturbed electrostatic potential $\delta\phi$, the perturbed vector potential $\delta A_\parallel$, and the perturbed parallel current $\delta J_\parallel$ for two different resistivity cases. The blue dashed lines represent the boundaries of the tearing layer with $\eta = 1.8 \times 10^{-6}\,\Omega \cdot m$, and the yellow dashed lines represent the boundaries of the tearing layer with $\eta = 4.5 \times 10^{-7}\,\Omega \cdot m$.

pressure gradient term into the parallel electron force balance equation to capture the effects of diamagnetic drift on tearing modes, which lead to the emergence of drift-tearing modes, for the first time. The reduced MHD version of this model, i.e., the gyro-MHD equations,

which are different from the previous two-fluid simulation model, is verified through simulations of linear resistive tearing modes and drift-tearing modes in a cylindrical geometry. We verify the resistive tearing mode simulations by scanning the values of the plasma beta to observe the corresponding changes in the growth rate and radial mode width. The scaling relation between the growth rate and the beta value when the equilibrium magnetic field is varied agrees well with the theoretically predicted relation $\gamma \sim \beta^{-1/5}$. The influence of the equilibrium pressure gradient, which results in drift-tearing mode formation, is also investigated. Drift-tearing modes arise from the coupling of drift modes and tearing modes, which leads to a real frequency equal to the electron diamagnetic frequency and a reduction in the growth rate. The width of the current layer is also broadened by the effects of the equilibrium pressure gradient. The scaling relation between the diamagnetic frequency and the growth rate of the drift-tearing mode agrees well with the theoretical prediction when the resistivity is relatively small, while a distinct discrepancy arises at larger resistivity values. In a sense, this discrepancy originates from the error introduced by adopting the constant-$\psi$ assumption in the theoretical derivation when the width of the tearing layer is large. The effects of kinetic ions and a toroidal geometry on drift-tearing modes will be studied in future work.

## REFERENCES

[1] H. P. Furth, J. Killeen, and M. N. Rosenbluth, Phys. Fluids **6**, 459 (1963).

[2] H. P. Furth, P. H. Rutherford, and H. Selberg, Phys. Fluids **16**, 1054 (1973).

[3] P. H. Rutherford, Phys. Fluids **16**, 1903 (1973).

[4] R. B. White, Rev. Mod. Phys. **58**, 183 (1986).

[5] F. Perkins, D. Post, N. Uckan, M. Azumi, D. Campbell, N. Ivanov, N. Sauthoff, M. Wakatani, W. Nevins, M. Shimada et al., Nucl. Fusion **39**, 2137 (1999).

[6] K. Ikeda, Nucl. Fusion **50**, 014002 (2010).

[7] A. B. Hassam, Phys. Fluids **23**, 2493 (1980).

[8] D. Li, Phys. Plasmas **2**, 3275 (1995).

[9] R. D. Hazeltine, D. Dobrott, and T. S. Wang, Phys. Fluids **18**, 1778 (1975).

[10] J. F. Drake and Y. C. Lee, Phys. Fluids **20**, 1341 (1977).

[11] M. Rosenberg, R. R. Dominguez, W. Pfeiffer, and R. E. Waltz, Phys. Fluids **23**, 2022 (1980).

[12] D. Biskamp, Nucl. Fusion **18**, 1059 (1978).

[13] D. A. Monticello and R. B. White, Phys. Fluids **23**, 366 (1980).

[14] Q. Yu, S. Günter, and B. D. Scott, Phys. Plasmas **10**, 797 (2003).

[15] B. D. Scott, J. F. Drake, and A. B. Hassam, Phys. Rev. Lett. **54**, 1027 (1985).

[16] A. I. Smolyakov, Plasma Phys. Controlled Fusion **35**, 657 (1993).

[17] Q. Yu, Nucl. Fusion **50**, 025014 (2010).

[18] H. Cai and G. Fu, Phys. Plasmas **19**, 072506 (2012).

[19] D. Brennan, C. Kim, and R. L. Haye, Nucl. Fusion **52**, 033004 (2012).

[20] W. W. Lee, Phys. Fluids **26**, 556 (1983).

[21] I. Holod, W. L. Zhang, Y. Xiao, and Z. Lin, Phys. Plasmas **16**, 122307 (2009).

[22] D. Liu, W. Zhang, J. Mcclenaghan, J. Wang, and Z. Lin, Phys. Plasmas **21**, 122520 (2014).

[23] H. Feng, W. Zhang, C. Dong, J. Cao, and D. Li, Phys. Plasmas **24**, 102125 (2017).

[24] W. A. Hornsby, P. Migliano, R. Buchholz, L. Kroenert, A. Weikl, A. G. Peeters, D. Zarzoso, E. Poli, and F. J. Casson, Phys. Plasmas **22**, 022118 (2015).

[25] Y. Chen, J. Chowdhury, N. Maksimovic, S. E. Parker, and W. Wan, Phys. Plasmas **23**, 056101 (2016).

[26] S. Nishimura, M. Yagi, S.-I. Itoh, M. Azumi, and K. Itoh, J. Phys. Soc. Jpn. **76**, 064501 (2007).

[27] S. Nishimura, S. Benkadda, M. Yagi, S.-I. Itoh, and K. Itoh, Phys. Plasmas **15**, 092506 (2008).

[28] W. Deng, Z. Lin, and I. Holod, Nucl. Fusion **52**, 023005 (2012).